Chapter 7

Simulations and Commented Results

7.1 Simulation schemes

In this section we consider the alternative configurations to evaluate our PD algorithm and present the final simulated schemes. Previously, in section 6.1.1, we took into account the convenience of performing the estimation of the inverse HPA characteristics in a post-distortion stage rather than in a simple pre-distortion one. According to this, the pre-distortion architectures presented here are basically derived from a post-distortion adaptive structure which may employ two general alternatives for its operation as shown in figure 7.1. These alternatives are:

1. Loading the pre-distorter with completely trained coefficients after a complete learning stage.

2. Simultaneous updating of the pre-distorter during the adaptation at the post-distortion loop.

The second system architecture enumerated above has been recently named "translation method" [66] and, for the present case, features some advantages for the design and operation of the PD techniques under evaluation. In the lower scheme of figure 7.1 we can observe that, as the adaptation error $\mathbf{e}$ converges to lower values, the adaptive pre-distorter should gradually approach the inverse gain characteristic of the HPA. Thence, the PDF of the input signal to the adaptive post-distorter will vary during the training process so that, when the best estimation is achieved, the PDF of $|\mathbf{b}_{in}|$ and the PDF of $|\mathbf{b}_y|$ are expected to be almost the same. This is of major importance for the correct application of the ELASTIC algorithm since it optimizes the centroids according to the probability distribution of the input data to the PD block. Therefore, since the objective is to apply pre-correction over $\mathbf{b}_{in}$, it is expected that the centroids be optimized at the post-distorer for a PDF as similar as possible to the input signal PDF.

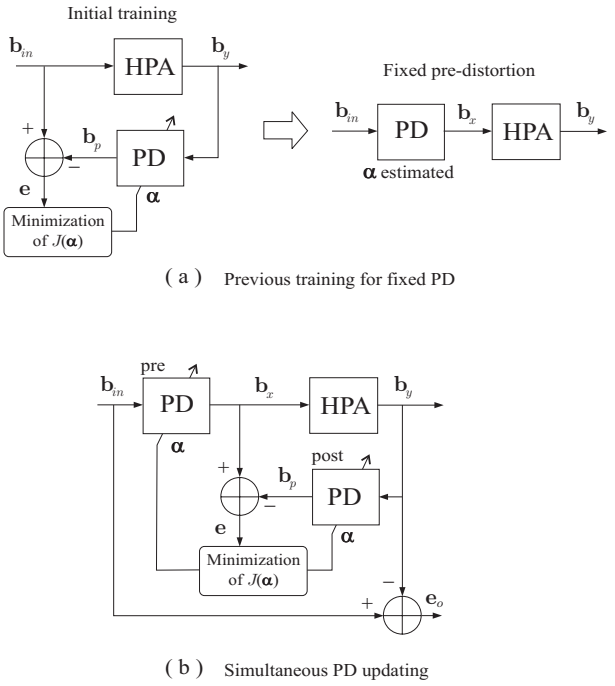

Figure 7.1: Basic alternatives to configure the process of PD adaptation and execution. (a) Training stage previous to fixed PD application on the transmission chain. (b) The estimated PD coefficients at the adaptive post-distorter are transferred at each iteration to the pre-distorter allowing permanent monitoring after coefficients convergence.

In the system of figure 7.2 the PD gain coefficients $\boldsymbol{\alpha}$ and the centroids $\mathbf{c}$ are trained at the adaptive post-distortion block according to the alternate adaptation procedure described in section 6.2. In this figure, the PD gain estimation and adaptive centroid reallocation processes are activated in alternate learning steps. Nevertheless, an important initial condition must be fulfiled for the right operation of the centroid reallocation algoritm, that is, the complex PD gain coefficients should be trained to fit the inverse gain curve previous to initiating the centroid adaptation. The reasons for this requirement clearly arise from the simulation results and are explained in the final sections.

Adaptive schemes based on the configurations in figures 7.1 and 7.2 were implemented with a basic random signal generator which provided the Rayleigh distributed data to represent, in simplified form, the expected input of an OFDM base-band signal. In figure 7.3 we show the probability distributions of the input signal modulus for different input power levels tested. A table with the corresponding IBO values is included in order to provide a more illustrative reference for the IBO levels used in some simulations. This basic signal generation allowed us to perform long tests to determine the average limits of the linearization performance which are contrasted with the theoretical bound found in section 5.2.1 for an ideal linear limiter. Along with the exaustive averaging, some independent results using simple estimation of gain coefficients and joint adaptation of gain coefficients and centroids are also provided.

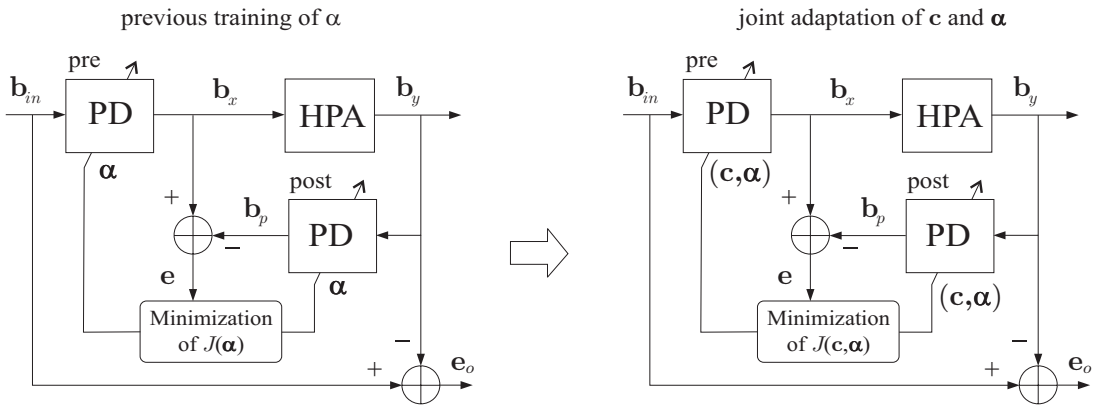

Figure 7.2: Required training sequence and adaptive configuration for joint estimation of PD gain and centroid distribution using ELASTIC. At each iteration, an input signal block $\mathbf{b}_{in}$ of length $N = 128$ is fed into the system. The input signal statistics correspond to a two-dimensional complex gaussian process with mean power $2\sigma^2$. Therefore, the amplitude samples in $|\mathbf{b}_{in}|$ correspond to a Rayleigh distribution according to (5.2) and (5.3), while the phase components $\arg\{\mathbf{b}_{in}\}$ are uniformly distributed in $[-\pi, \pi]$. The adequate training sequence considers a previous adaptation of the PD gain coefficients α with an initial uniform distribution of fixed centroids. After a first convergence, the 2-D position of the interpolation coefficients inform about the general morphology of the inverse gain curve. Under such conditions, the ELASTIC algorithm can optimize the centroid positions following the local variations along the curve and the activation probability of the resulting intervals at each iteration.

The evaluation of the PD techniques presented in this work was also extended to a more complete system by implementing the simulation of a basic OFDM transmission chain which is shown in figure 7.4. The transmission chain was implemented as a base-band equivalent according to the general parameters for OFDM generation tabulated below.

OFDM signal generation parameters	
Modulation levels	Q-PSK, 16-QAM and 64-QAM
Total number of subcarriers	64
Active subcarriers	52
Null subcarriers	12
Cyclic prefix/symbol duration	1/4
Interpolation ratio at IFFT (zero padding)	2
D/A oversampling ratio	16

The signal constellations generated before the IFFT modulation are shown in figure 7.6. In the system of figure 7.4, signal blocks of 64 symbols from these constellations are first zero padded resulting in blocks of length 128 that are given to the IFFT block. The PSD of the signal at this point (IFFT output) is shown in figure 7.7. The effect of the nonlinear distortion and its compensation through the proposed PD scheme is shown for

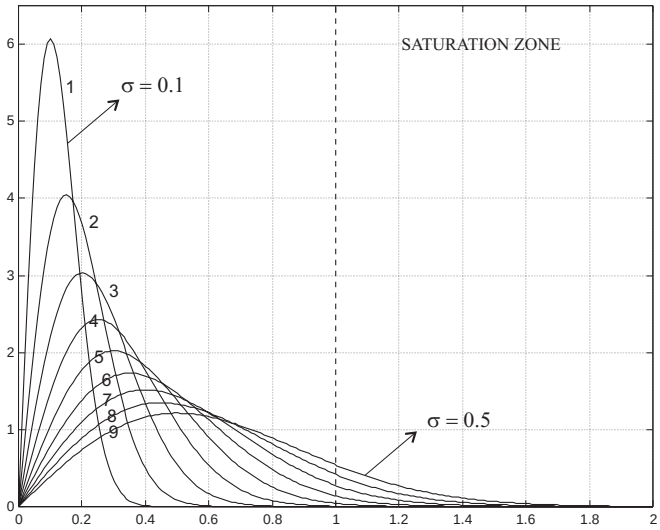

	σ	IBO_{dB}	p_{sat}
1	0.1	16.99	1e-20 %
2	0.15	13.06	1e-7 %
3	0.20	10.78	0.0006 %
4	0.21	10.37	0.002 %
5	0.27	8.31	0.1 %
6	0.32	6.65	1 %
7	0.38	5.26	3.47%
8	0.44	4.06	7.8 %
9	0.5	3.01	13.53 %

Figure 7.3: PDFs for different tested values of input power expressed through IBO.

the data correction at the reception as well as for the power spectral densities at different points along the signal path. In the system of figure 7.4, we show the training structure implemented where the pre-distorter and the D/A filter are optionally activated with s_1 and s_2. For the case in which the filter h_1 is activated, a block for time alignment with a discrete resolution step of $\Delta T_s = T_s/32$ is included to compensate almost all the time delay introduced by h_1. However, the remaining uncompensated fractional delay and the band-limitting effect of the filter will appear along the chain as degrading effects for nonlinear distortion compensation and, therefore, its influence shall be evaluated.

In figure 7.5 we show the system structure for testing the PD gain previously estimated using the learning structure of figure 7.4. The improvement introduced at the linearized chain (upper branch) by applying the estimated PD can be thus measured with respect to the nonlinear distorted transmission (lower branch) by observing the in-band and out-of-band compensations as well as measuring the I/O error spectrum levels achieved for each given number of coefficients or centroids used for PD and with respect to the input power (IBO) defined for the signal at the transmission end. For the observation of the I/O error we considered the inclusion of a compensation block embedding all the linear processing present along the transmission path. This is done in order to eliminate the observation of the in-band distortion components resulting from the uncompensated delays due to the D/A–A/D conversion. This compensation is, of course, arbitrary and solely intended to allow the observation of the nonlinear compensation isolated from other error sources.

The results herein presented were obtained for the PD gain optimization algorithms described in sections 6.1.5 and 6.2. In the adaptive systems implemented, two MSE measures were considered: the first one is based on the adaptation error signal $\mathbf{e} = \mathbf{b}_x - \mathbf{b}_p$ and the second one is based on the measured I/O error signal $\mathbf{e}_o = \mathbf{b}_{in} - \mathbf{b}_y$. The latter one is the final measure of goodness which will serve as a reference in evaluating the benefits achieved with linearization. These measures are both normalized with respect to

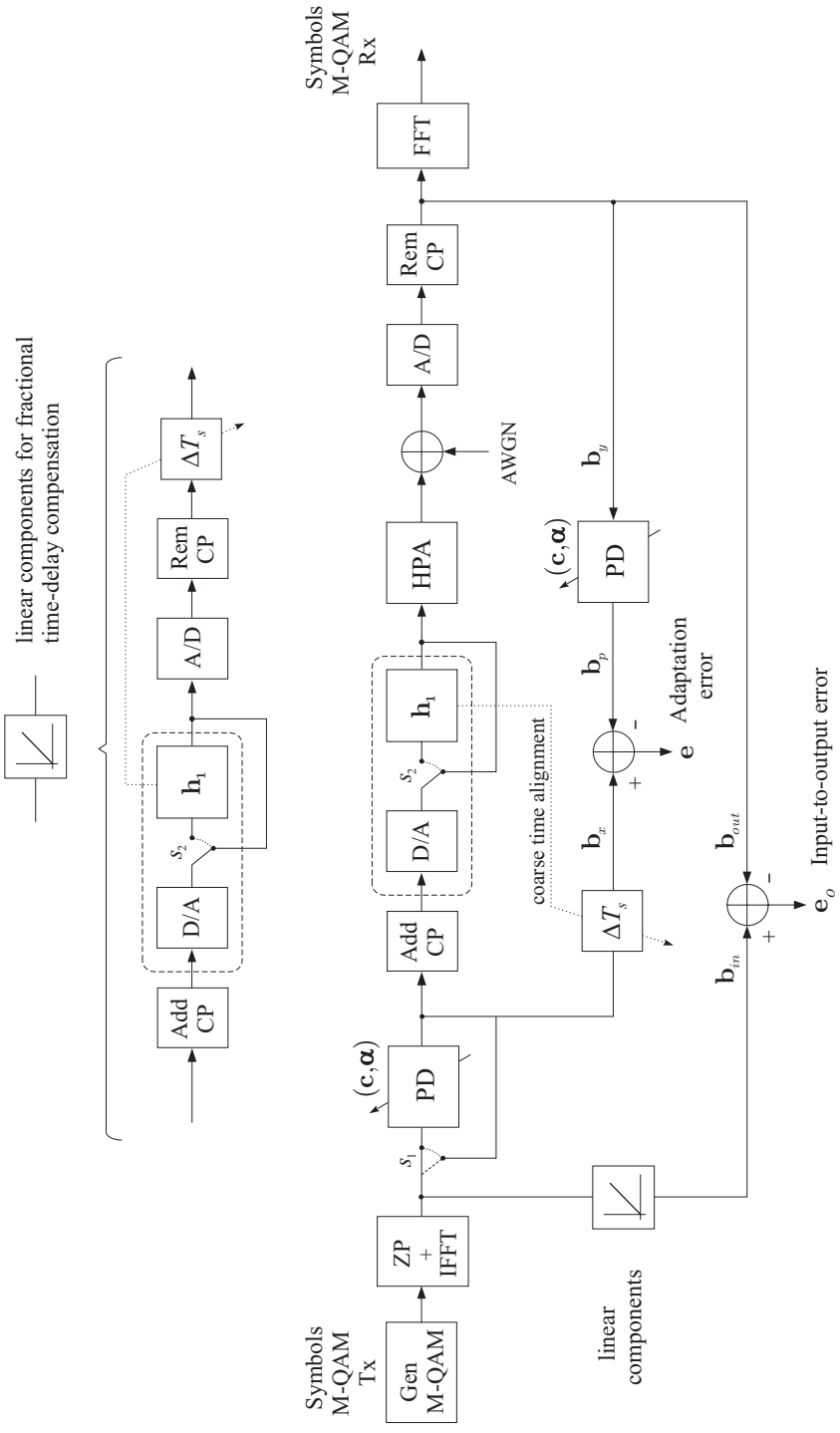

Figure 7.4: Basic OFDM chain implemented for the evaluation of the PD algorithms.

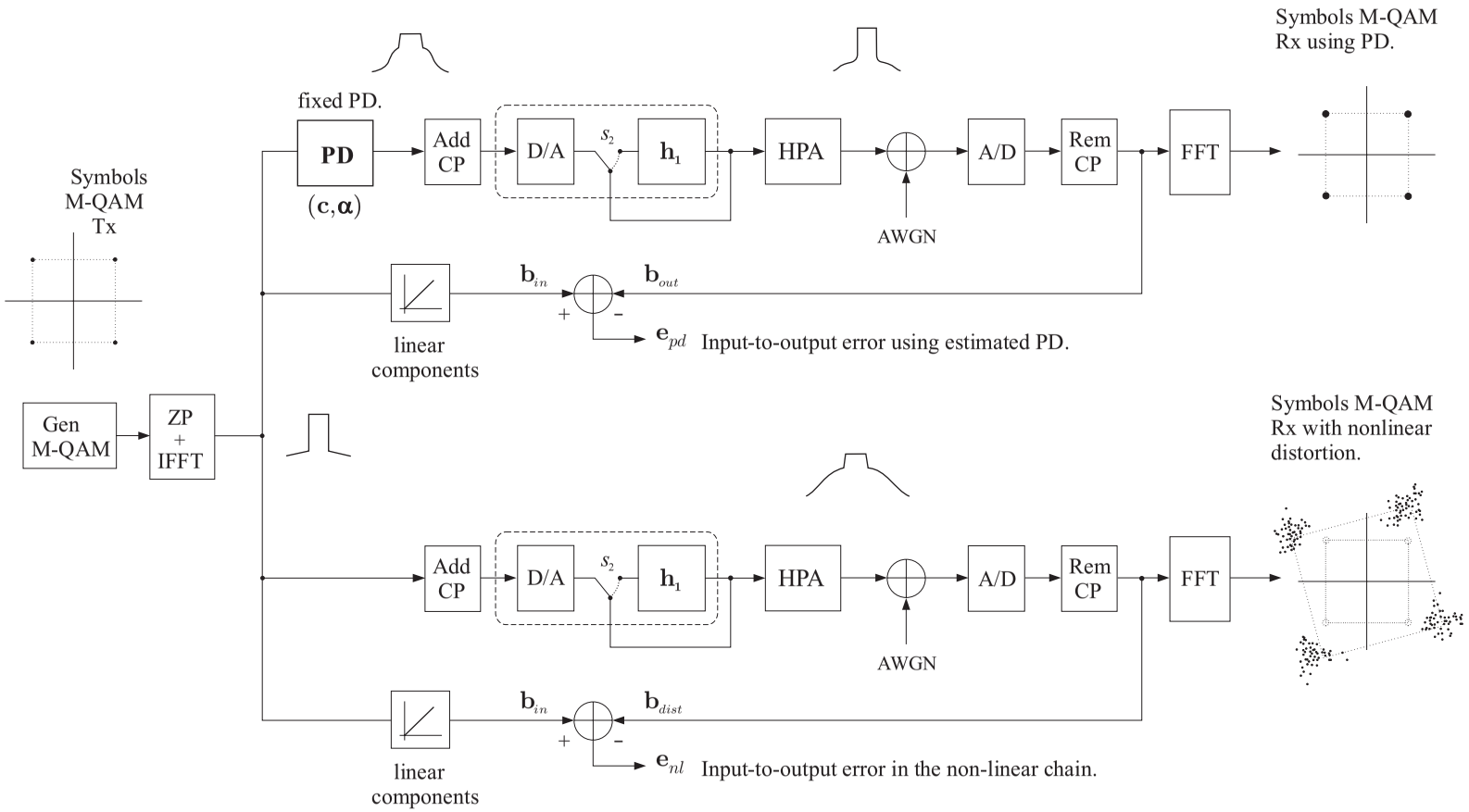

Figure 7.5: Linearized and nonlinear transmission chains implemented for evaluating the estimated pre-distorter.

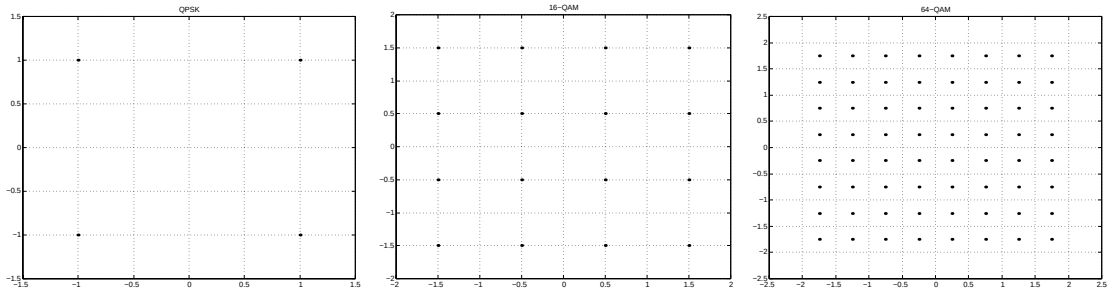

(a) QPSK (b) 16-QAM (c) 64-QAM

Figure 7.6: Symbol constellations generated for the OFDM transmission.

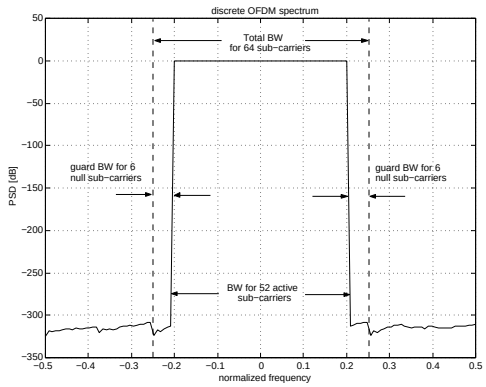

Figure 7.7: Power spectral density of the input discrete OFDM signal generated with 52 active and 12 null orthogonal subcarriers.

the input signal power and calculated at each iteration as

$$E[n] = 10\log_{10}\frac{P_e[n]}{P_{in}[n]}$$
$$E_o[n] = 10\log_{10}\frac{P_{e_o}[n]}{P_{in}[n]}$$

where

$$P_e = \frac{1}{N}\mathbf{e}^H\mathbf{e}\ ;\ P_{e_o} = \frac{1}{N}\mathbf{e}_o^H\mathbf{e}_o \text{ and } P_{in} = \frac{1}{N}\mathbf{b}_{in}^H\mathbf{b}_{in}$$

with N=128, the length of the signal blocks. The updating equation (6.43) has been slightly modified by including an estimation of the mean input power, $\overline{P}_{in} = (1/N)\cdot\mathbf{b}_{in}^H\mathbf{b}_{in}$, as a normalization factor to the adaptation step μ_α. Hence, the adaptation of the PD gain coefficients is performed according to

$$\boldsymbol{\alpha}_{(n+1)} = \boldsymbol{\alpha}_{(n)} + \frac{\mu_\alpha}{\overline{P}_{in}}\boldsymbol{\Lambda}^T(\mathbf{b}_y^* \odot \mathbf{e}). \tag{7.1}$$

Similarly, the equation (6.73) for the adaptation of the intermediate parameters δ_k, which ultimately define the centroid adaptation, is also evaluated as a NLMS update given by

$$\boldsymbol{\delta}_{(n+1)} = \boldsymbol{\delta}_{(n)} - \frac{\mu_\delta}{\overline{P}_{in}}\widehat{\nabla}_{\delta_i}J(\mathbf{c}). \tag{7.2}$$

7.2 Simulation Results

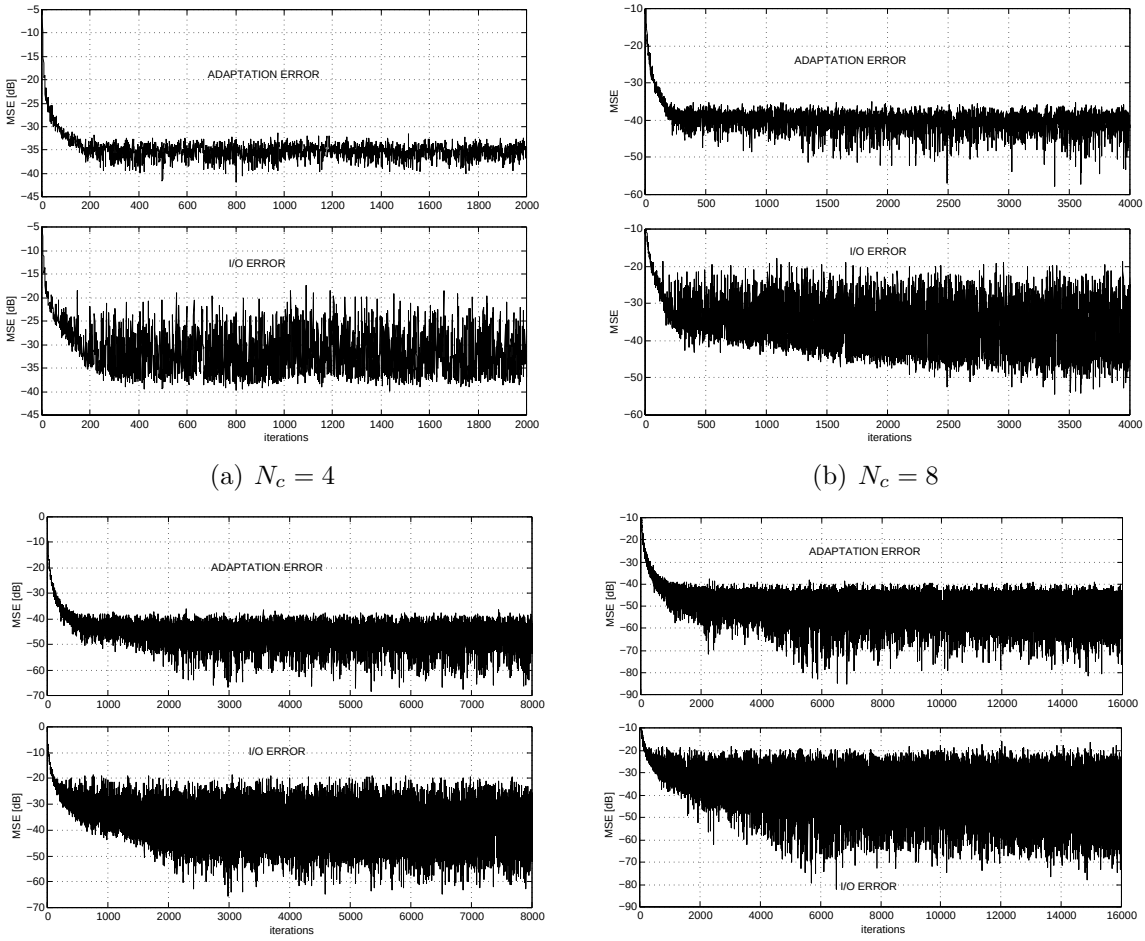

(a) $N_c = 4$ (b) $N_c = 8$

(c) $N_c = 16$ (d) $N_c = 32$

Figure 7.8: Evolution of the MSE for the adaptation error signal measured in the system of figure 7.1(b) for different numbers of interpolation coefficients with uniform fixed centroid distribution. An input signal with Rayleigh distributed envelope and with IBO = 6.65[dB] ($\sigma = 0.3286$) has been applied in all cases, which implies an approximate 0.1% of clipping probability. The adaptation step used in all cases is $\mu_\alpha = 0.002$. The MSE evolution has not been averaged in order to observe the high peak to average error ratio which is due to the high PAPR that characterizes a Rayleigh envelope.

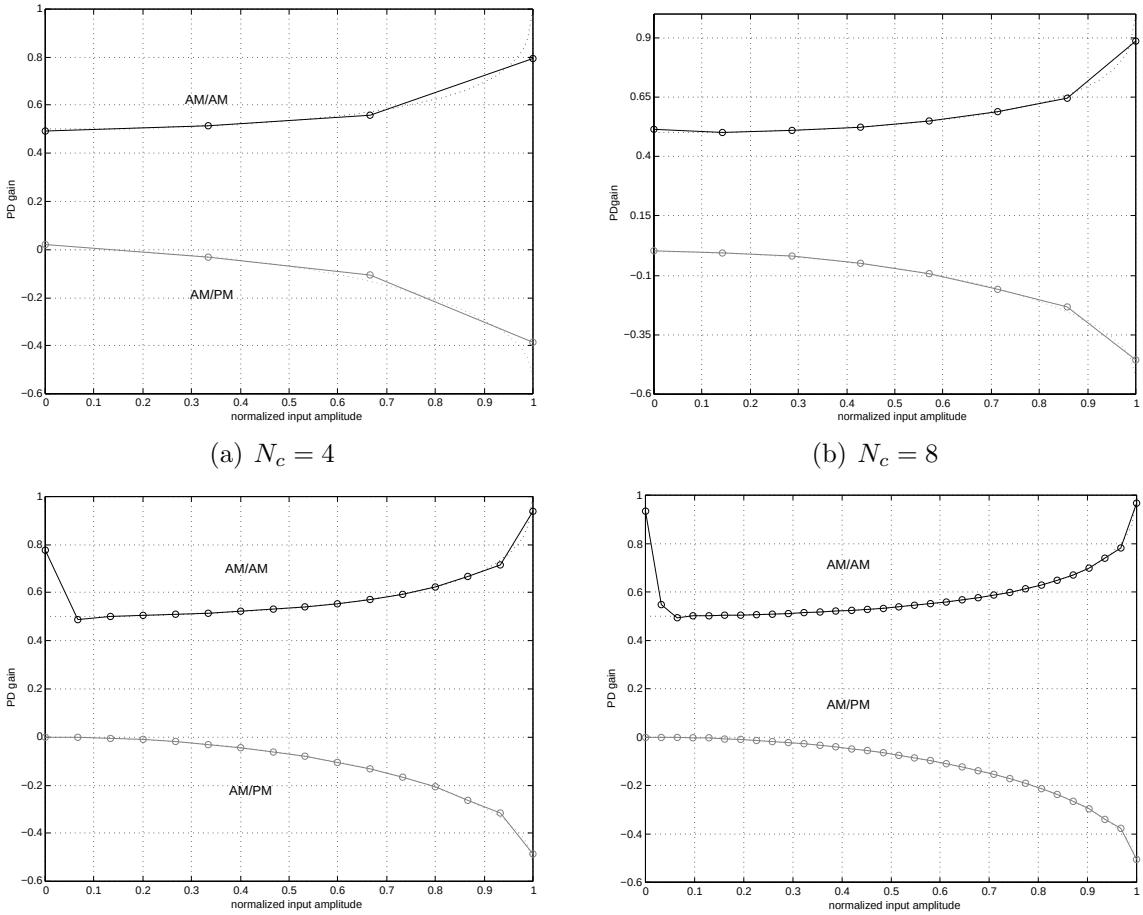

(a) $N_c = 4$ (b) $N_c = 8$

(c) $N_c = 16$ (d) $N_c = 32$

Figure 7.9: Estimated PD gain coefficients for the convergence levels shown in figure 7.8. The theoretical PD gain characteristics, calculated from eqs.(2.39) and (2.40), are shown in dotted line for reference. The circles mark the estimated PD coefficients related to the uniformly distributed centroids. Note that in the case of $N_c = 16$ and $N_c = 32$, although we considerably extended the adaptation time, the first coefficients still require many iterations to converge to the correct values. This occurs because of the low activation probability associated to the first intervals which become even lower as we divide this low probability region into more activation intervals.

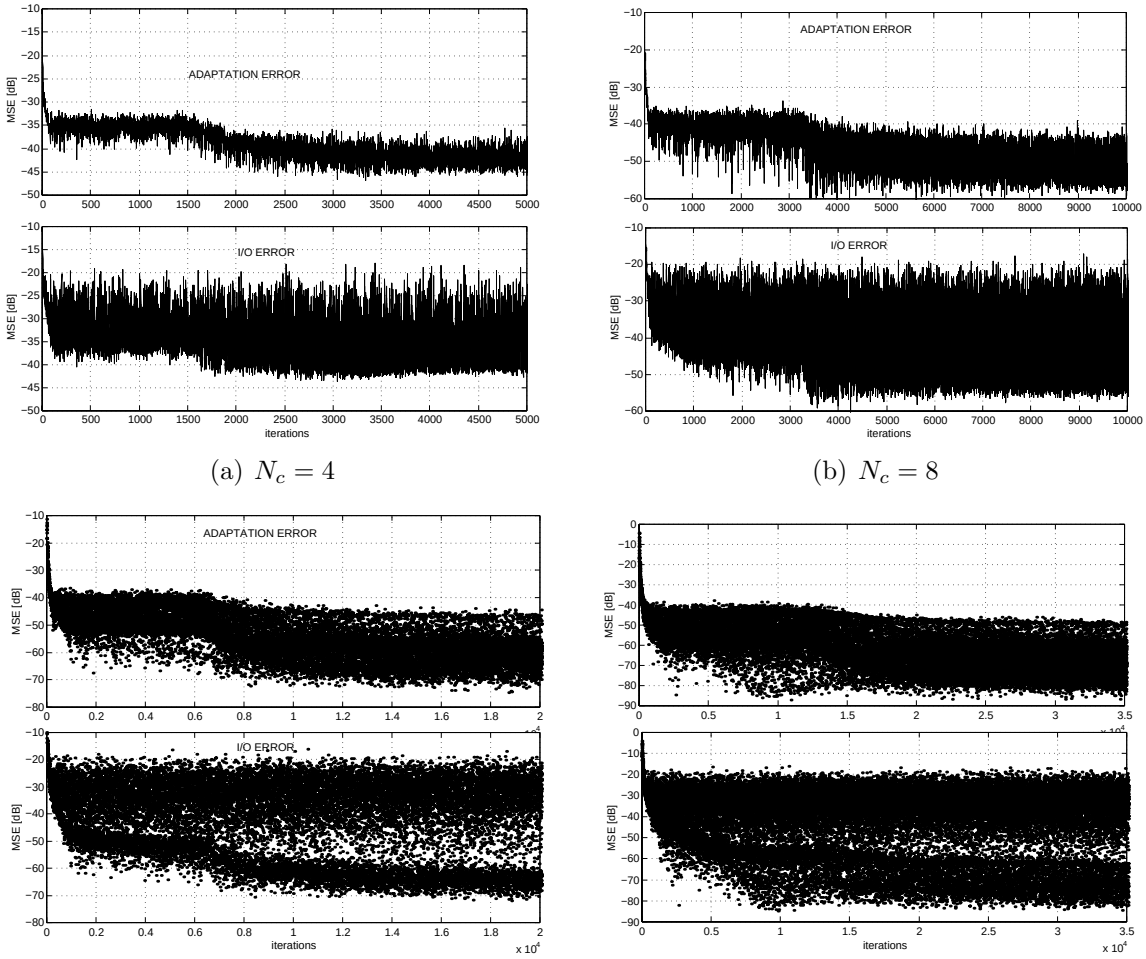

(a) $N_c = 4$

(b) $N_c = 8$

(c) $N_c = 16$

(d) $N_c = 32$

Figure 7.10: Evolution of the MSE for the adaptation error signal measured in the system of figure 7.1(b) for different numbers of interpolation coefficients with centroid reallocation using the ELASTIC algorithm from section 6.2.2. The same input signal used to obtain the MSE graphs in figure 7.8 is used here, i.e. Rayleigh distributed with IBO = 6.6563[dB] ($\sigma = 0.3286$). The adaptation step used in all cases is $\mu_\alpha = 0.002$ for gain coefficients adaptation and $\mu_\delta = 0.5$ for centroid adaptation. Note that the centroid reallocation starts at different times in each case to allow the gain coefficients to converge to a first estimation of the curve.

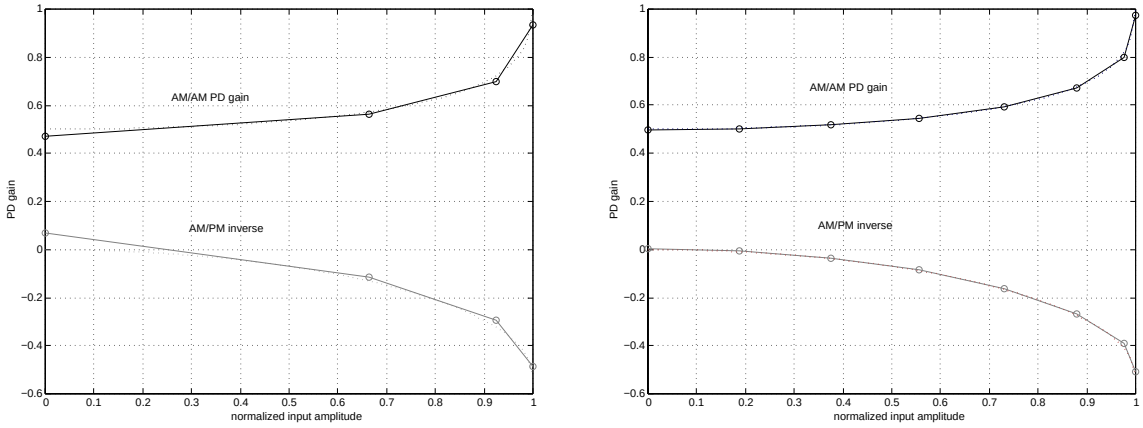

(a) $N_c = 4$

(b) $N_c = 8$

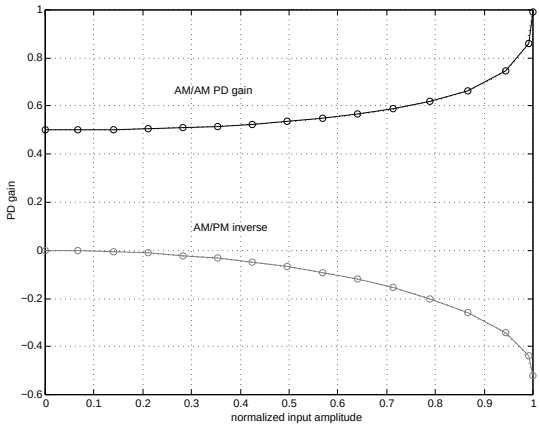

(c) $N_c = 16$

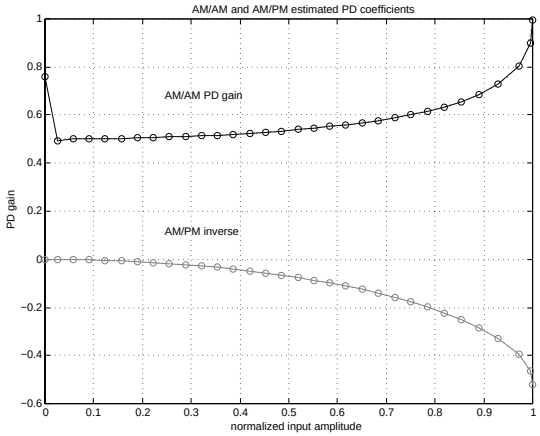

(d) $N_c = 32$

Figure 7.11: Estimated PD gain coefficients for the convergence levels shown in figure 7.10. The theoretical PD gain characteristics, calculated from eqs.(2.39) and (2.40), are shown in dotted line for reference. The circles mark the estimated PD coefficients related to the reallocated centroids. Note that for the case of $N_c = 32$ the first coefficient is far from its optimum value due to the low probability of activation of the first interval. This suggests that starting the learning process with an excess of coefficients should be avoided. Instead, increments in the resolution based on a first estimation using few coefficients and wider intervals could be considered.

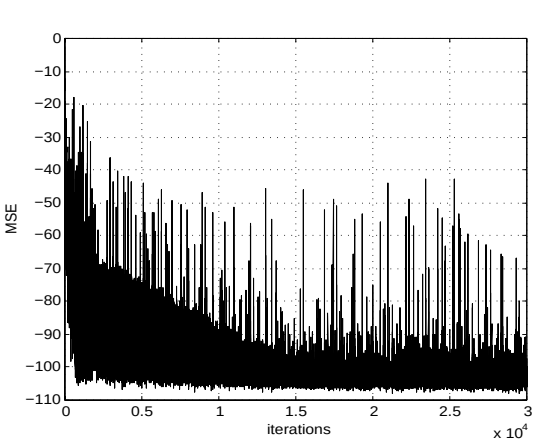

(a) $N_c = 64$

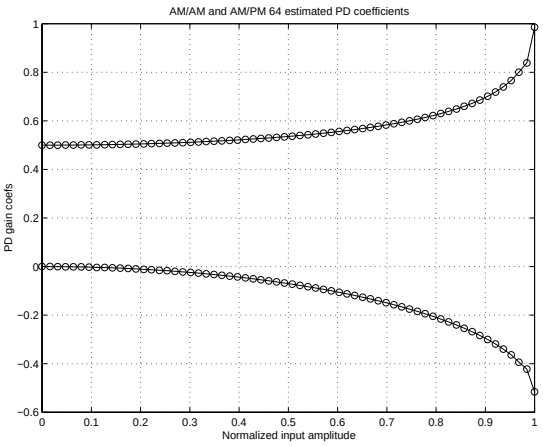

(b) $N_c = 64$

Figure 7.12: Evolution of the mean squared error and estimated PD coefficients for $N_c = 64$ uniformly distributed centroids. An adaptation step of $\mu = 0.005$ has been applied using the same signal as in the previous cases of figures 7.8 and 7.9. From these figures showing estimated sets of PD coefficients, we can suppose that centroid reallocation will not improve significantly the MSE for the cases where $N_c > 16$. Moreover the size of activation matrices used for PD estimation increases with the square of the number of coefficients. Thence, this last example for $N_c = 64$ is included as an illustration of the use of an excess of interpolation coefficients.

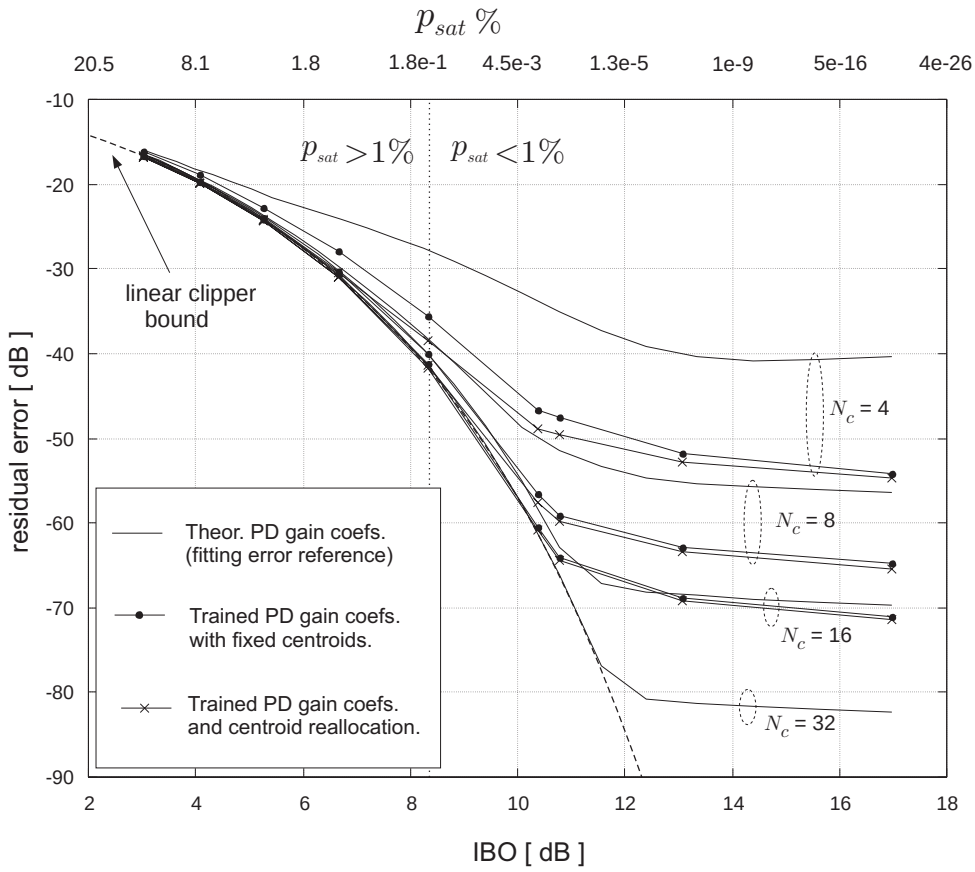

Figure 7.13: In this figure we show the results for the long term averaging of the residual error power for different values of IBO and different numbers of centroids. The residual error is the mean power of the I/O error signal $\mathbf{e}_0$ measured in PD systems using the structures shown in figures 7.1 and 7.2. This measure appears here in dB, normalized with respect to the mean input power $\overline{P}_{in} = 2\sigma^2$ which also defines the corresponding IBO values in the horizontal axis through the relation (5.11) for $A_{sat} = 1$. The theoretical reference lines for each case have been obtained by applying in the PD block the gain coefficients α calculated exactly from (2.39) and (2.40). This is obviously a sub-optimal reference because taking the coefficients from the theoretical PD gain curve and using them to perform linear interpolation introduces a fitting error that can only be reduced by augmenting significantly the number of centroids. Along with the theoretical curves for $N_c = \{4, 8, 16, 32\}$ centroids, we obtained the resulting residual errors, for the different number of uniformly distributed centroids now, however, using PD gain coefficients trained with the basic adaptive algorithm described in section 6.1.5, equation (6.43). Then, the same IBO values were used to find the average performance of the PD estimation including centroid reallocation with the ELASTIC algorithm. From the results we observe that in the highly saturated region (low IBO) the residual error level does not improve significantly with the number of centroids and, as the clipping distortion becomes more predominant, all the curves converge to the theoretical bound defined for the ideal limiter (clipper) in section 5.2.1 equation (5.21). Since the differences between the cases with and without centroid adaptation are not easily noticeable from these curves, next, in figure 7.14 we depict the numerical diference in dB. Finally, notice that higher IBO values represent lower input signal power.

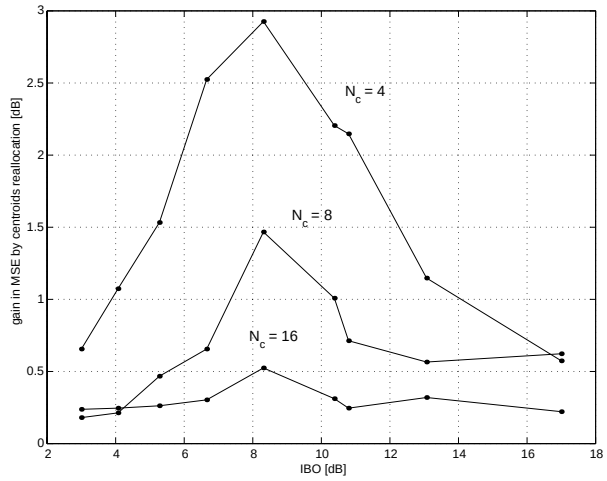

Figure 7.14: In this figure we depict the difference between the values of residual error obtained with and without centroid allocation for $N_c = \{4, 8, 16\}$ previously shown in figure 7.13. Here we observe that using the ELASTIC reallocation of centroids improves the residual error specially for a range of IBO around the 8[dB]. However, adaptive centroid reallocation does not improve significantly the error floor when the IBO is out of this range. This is quite reasonable since, on the one hand, lower values of IBO are in a highly saturated region where the clipping distortion will be predominant over any improvement of the error for input values within the valid input range of the HPA. On the other hand, the higher values of IBO mean that the signal power is too small and therefore only the lowest intervals may be activated. In such case, the distribution of the remaining centroids is irrelevant for the mean residual error.

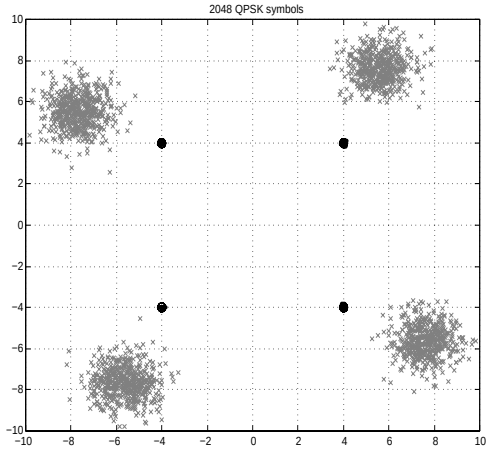

(a) QPSK correction

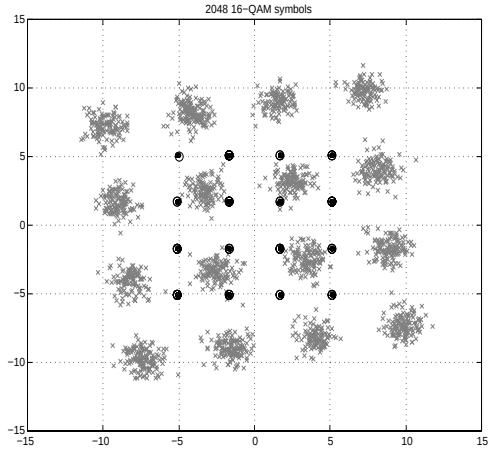

(b) 16-QAM correction

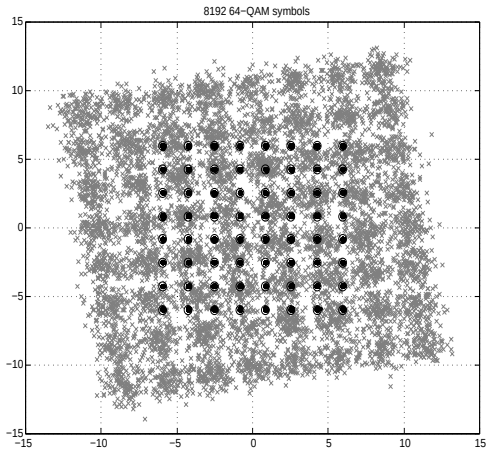

(c) 64-QAM correction

Figure 7.15: Examples of symbol constellations showing the data correction achieved with a reduced number of $N_c = 4$ PD gain coefficients with uniform centroid distribution. The 'x' correspond to the received symbols without linearization and show the typical effect introduced by a nonlinear HPA, that is, the Rx will observe a warped constellation of point clusters. The dark dots represent the received symbols using the estimated PD and the circles mark the exact positions of the Tx symbols. The learning structure shown in figure 7.4 was applied in each case generating an input OFDM signal with an IBO= 10dB. In this cases no filtering with $\mathbf{h}_1$ was applied. Note that all the symbol constellations included in this chapter correspond to the information transmitted through the same sub-carrier (from the set of 52 activated) for a sequence of OFDM symbols.

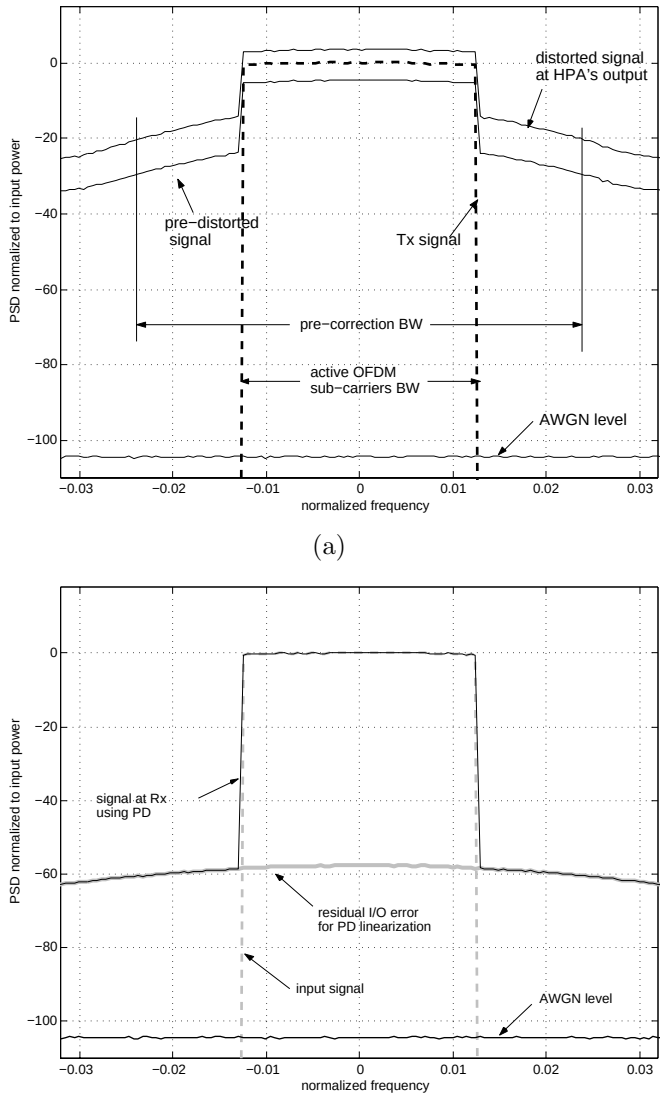

Figure 7.16: Example of linearization effects on the Power spectral densities for the system in figure 7.5. In this case, the linearization has been obtained using $N_c = 8$ PD coefficients estimated according to the adaptive structure in figure 7.4. The input signal has been set to an IBO= 8.96dB. In figure (a) we show the PSD of the distorted signal at the HPA output without using pre-distortion, that is, the HPA output at the lower branch in figure 7.5. The spectral regrowth observed corresponds completely to out-of band distortion components, while the observed in-band increment of near 3dB is due to a combination of linear and nonlinear gains introduced by the HPA which cannot be distinguished from spectral observations. In (a) we also observe the PSD resulting from pre-distorting the OFDM input signal. At the output of the pre-distorter we will observe the appearance of out-of-band components which are necessary to compensate for the out-of-band distortion introduced by the nonlinear gain at the HPA. Note that when analog filtering with $\mathbf{h}_1$ is applied after PD, the pass-band of the filter will define the "*pre-correction bandwidth*" since part of these out-of-band components that form the pre-distorted signal will be masked before the HPA input and, therefore, the final linearization result will be affected.

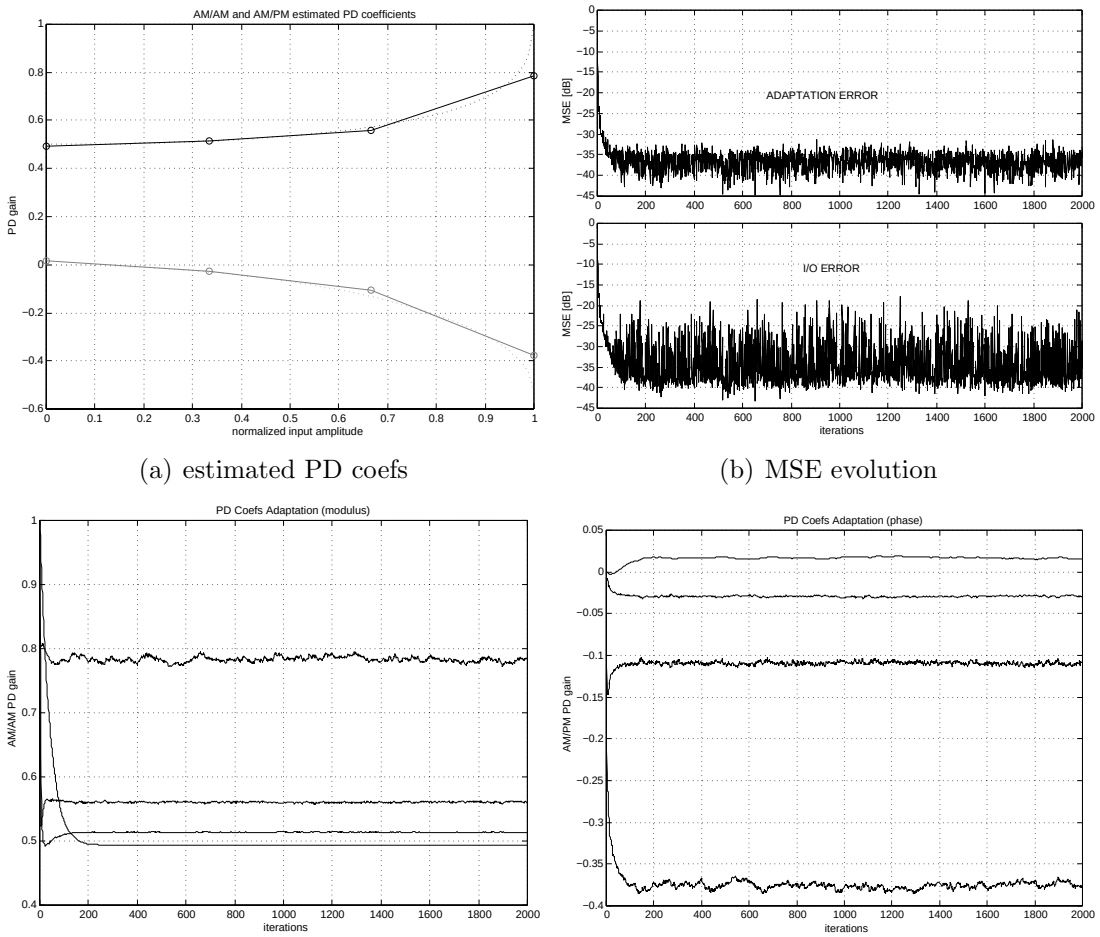

(a) estimated PD coefs

(b) MSE evolution

(c) AM/AM coefficients

(d) AM/PM coefficients

Figure 7.17: Results for a test with $N_c = 4$ coefficients with centroids fixed in a uniform distribution. In this case the filter $\mathbf{h}_1$ is bypassed. An input signal with Rayleigh distributed amplitude and with IBO = 7.027[dB] has been applied in this case, which implies a theoretical 0.65% of clipping probability. (a) Estimated PD coefficients. (b) Evolution of the adaptation and I/O error measured as shown in figure 7.4. (c) Evolution of the AM/AM and AM/PM coefficients estimated for PD. The adaptation step used was $\mu_\alpha = 0.005$.

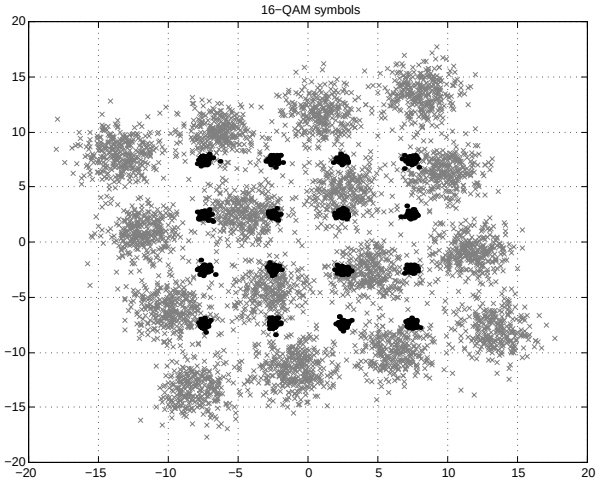

(a) Data correction

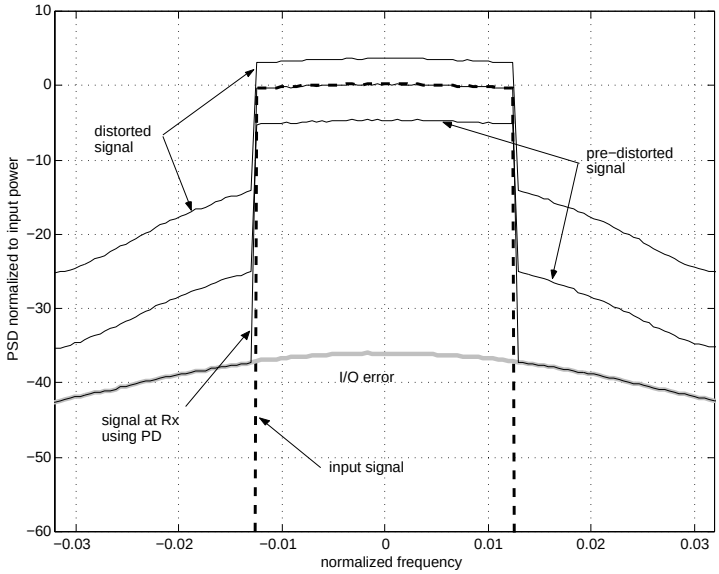

(b) PSD results

Figure 7.18: Results for the adaptation of $N_c = 4$ centroids with uniform distribution presented in figure 7.17

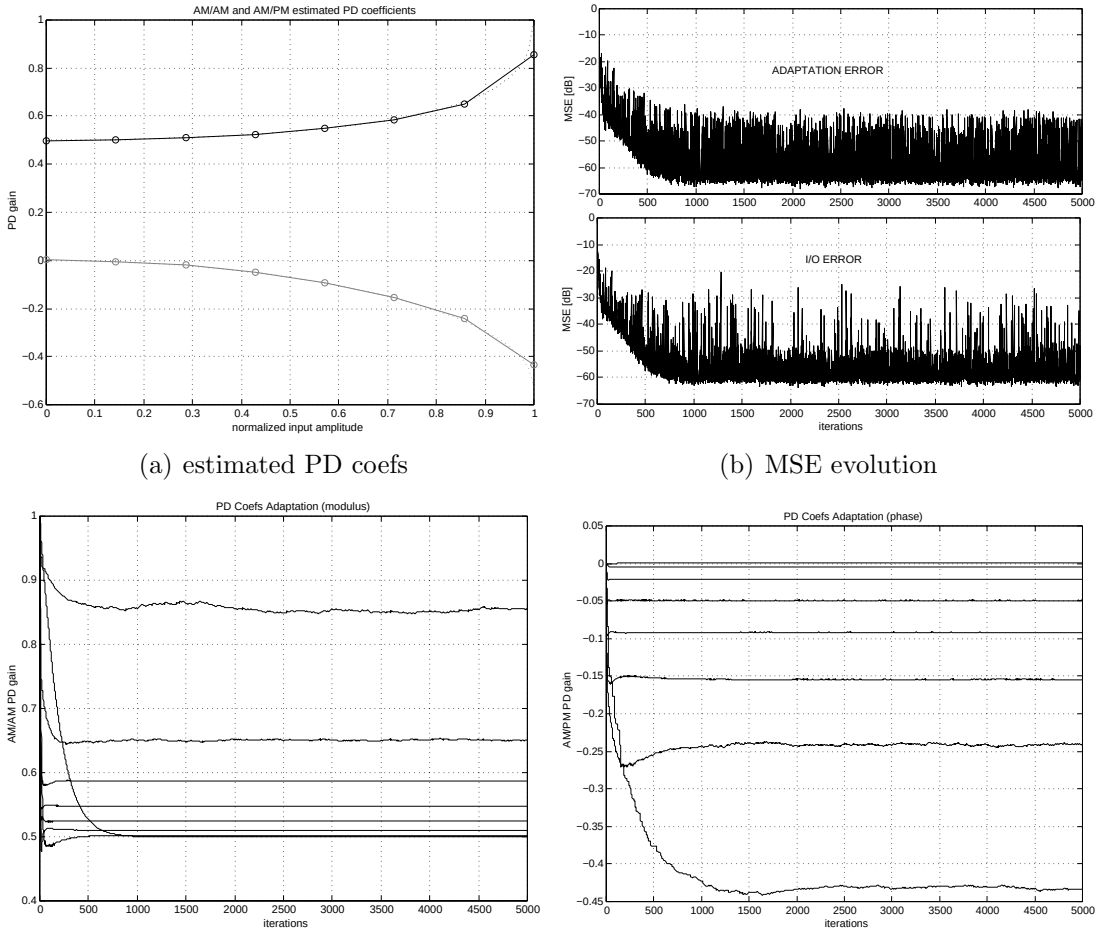

(a) estimated PD coefs

(b) MSE evolution

(c) AM/AM coefficients

(d) AM/PM coefficients

Figure 7.19: Results for a test with $N_c = 8$ coefficients with centroids fixed in a uniform distribution. In this case the filter $\mathbf{h}_1$ is bypassed. An input signal with (amplitude) Rayleigh distribution with IBO = 8.96[dB] ($\sigma = 0.252$) has been applied in this case, which implies a theoretical 0.04% of clipping probability.(a)Estimated PD coefficients.(b)Evolution of the adaptation and I/O error measured as shown in figure 7.4.(c)Evolution of the AM/AM and AM/PM coefficients estimated for PD. The adaptation step used was $\mu_\alpha = 0.005$.

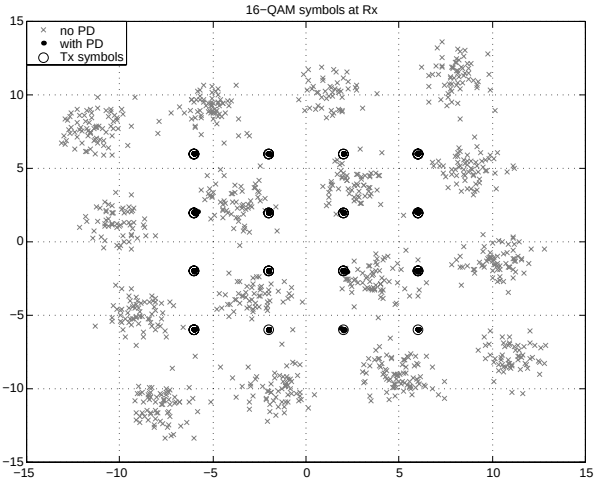

(a) Data correction

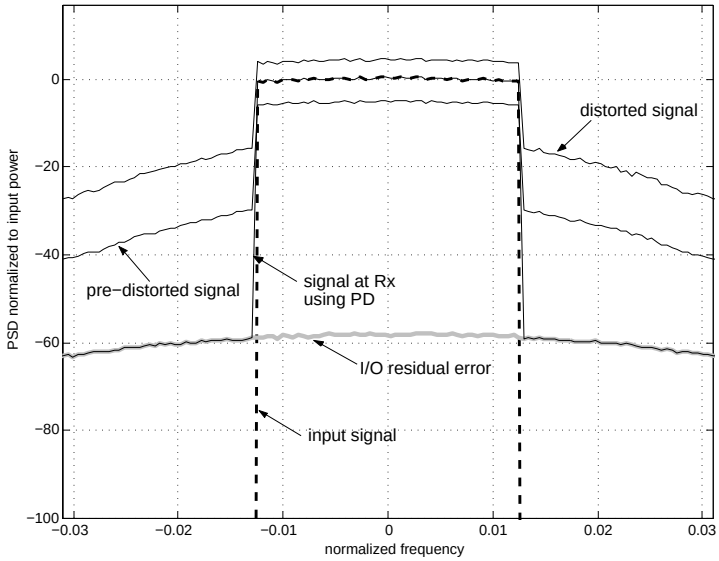

(b) PSD results

Figure 7.20: Results for the adaptation of $N_c = 8$ centroids with uniform distribution presented in figure 7.19

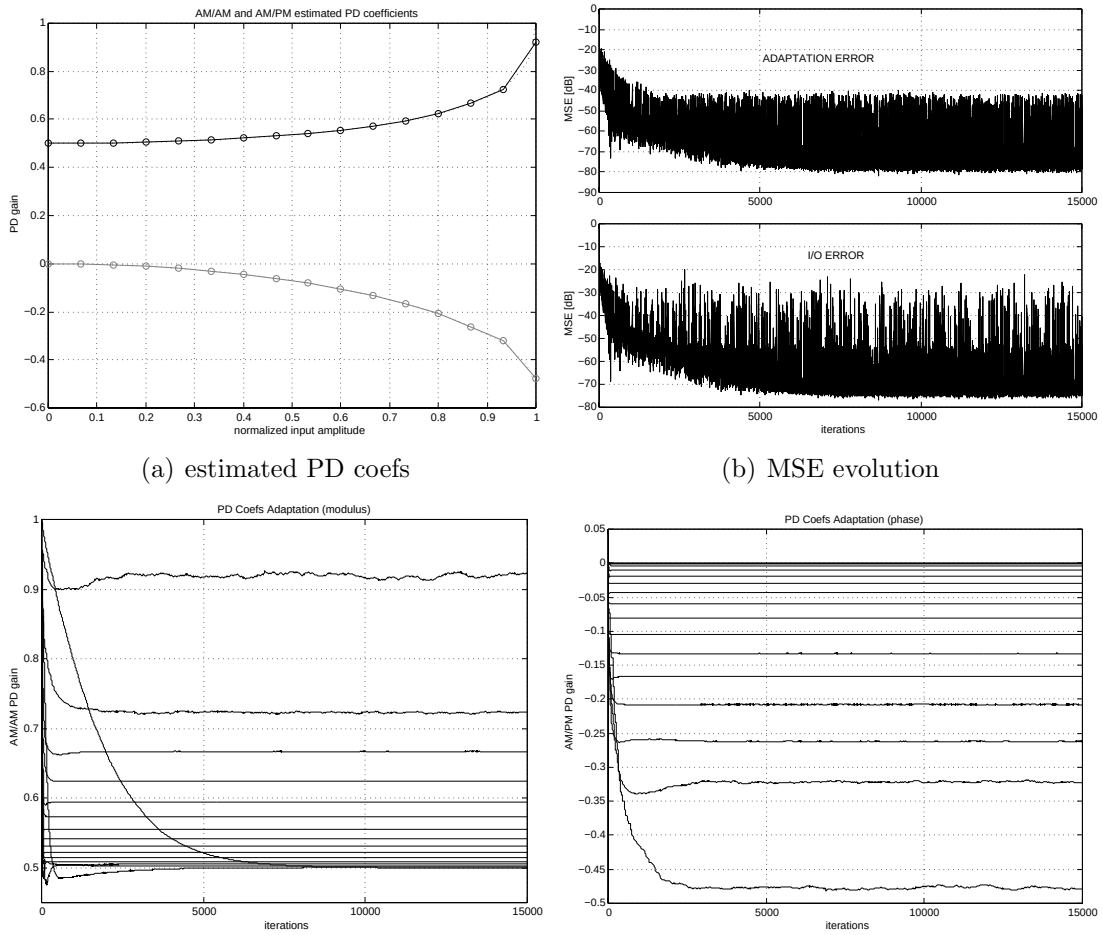

(a) estimated PD coefs

(b) MSE evolution

(c) AM/AM coefficients

(d) AM/PM coefficients

Figure 7.21: Results for a test with $N_c = 16$ coefficients with centroids fixed in a uniform distribution. In this case the filter $\mathbf{h}_1$ is bypassed. An input signal with (amplitude) Rayleigh distribution with IBO = 8.96[dB] has been applied in this case, which implies a theoretical 0.04% of clipping probability.(a)Estimated PD coefficients.(b)Evolution of the adaptation and I/O error measured as shown in figure 7.4.(c)Evolution of the AM/AM and AM/PM coefficients estimated for PD. The adaptation step used was $\mu_\alpha = 0.005$.

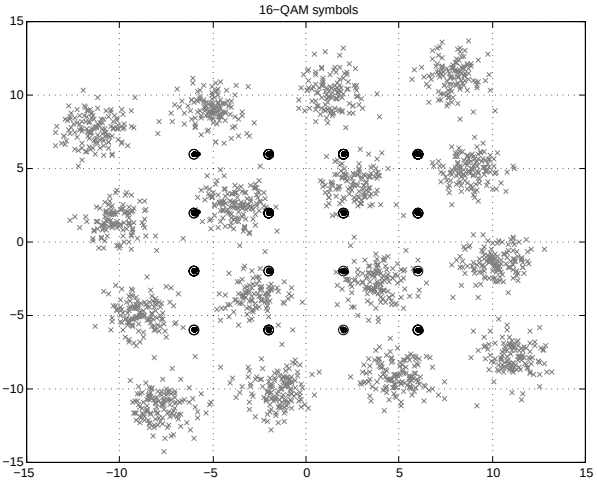

(a) Data correction

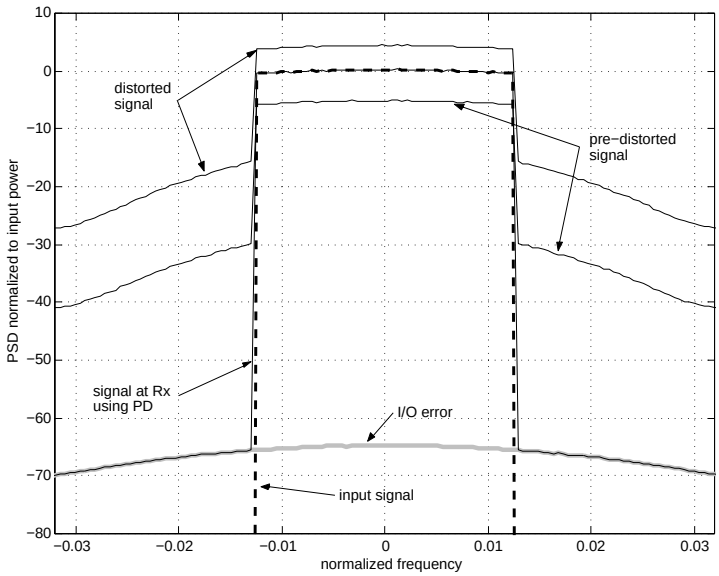

(b) PSD results

Figure 7.22: Results for the adaptation of $N_c = 16$ centroids with uniform distribution presented in figure 7.21

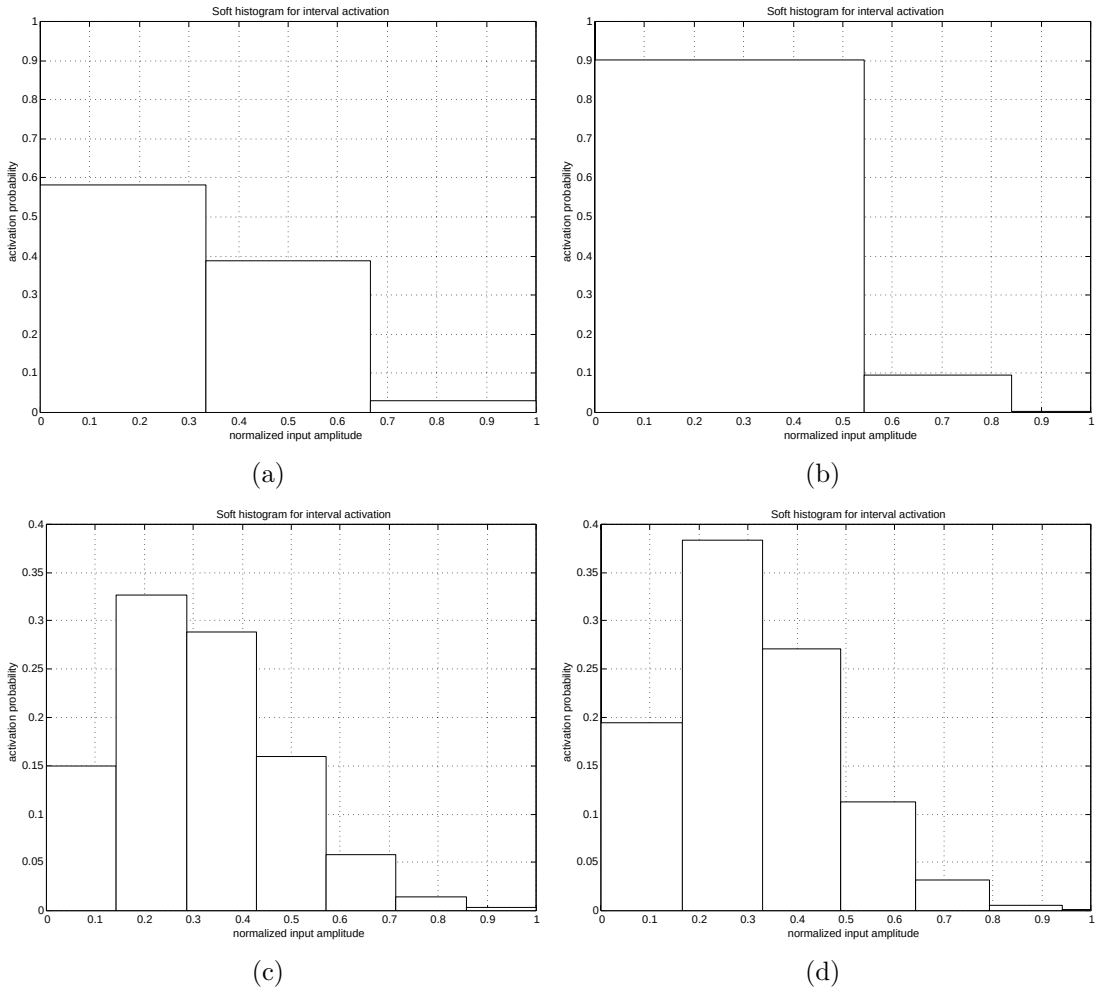

Figure 7.23: Interval activation probability obtained for the case of uniform distribution of centroids and after centroid reallocation using sets of $N_c = \{4, 8\}$ trained PD coefficients for an OFDM signal adjusted for an IBO=8.96dB at the output of the IFFT modulator in the upper branch of the system in figure 7.5. Note that, since the PD approaches the inverse characteristic of the HPA, the probability distributions in (b) and (d) are present at the post-distorter input. In figures (a) and (c) we observe the soft histograms for the activation probability of the intervals defined by $N_c = \{4, 8\}$ coefficients uniformly distributed. Then in figures (b) and (d) the same activation probability is shown considering the adapted set of 4 and 8 centroids respectively, which results in different interval widths and, therefore, different activation probabilities. The bar edges in these diagrams are defined by the centroid positions.

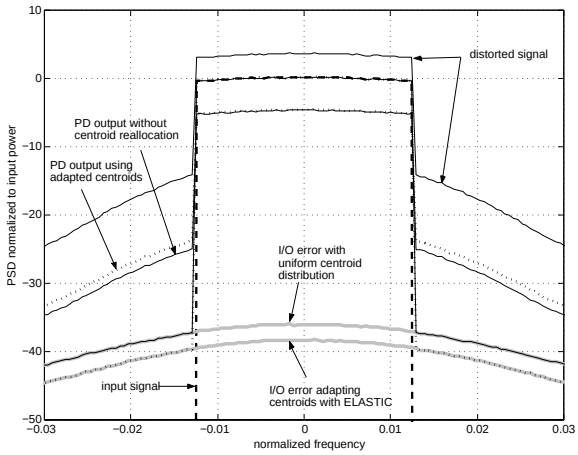

(a) Effect of the centroid reallocation on the PSD of figure 7.18(b)

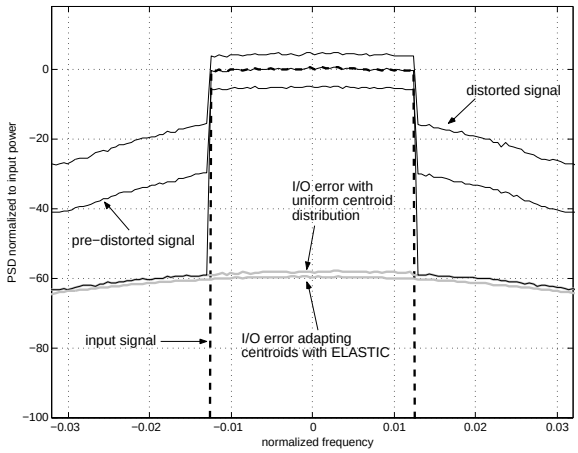

(b) Effect of the centroid reallocation on the PSD of figure 7.20(b)

Figure 7.24: In these figures we show the spectral results obtained using sets of $N_c = 4$ and $N_c = 8$ coefficients to pre-distort a signal with IBO= 7.027 and IBO= 8.96 respectively. The results were obtained using the training structure of figure 7.4 and then testing the estimated PD coefficients in the structure of figure 7.5. The same tests were carried out first using uniform sets of centroids and then using the adaptive centroid reallocation by means of the ELASTIC algorithm. The adaptation steps used in both cases where $\mu_\alpha = 0.005$ and $\mu_\delta = 0.5$. In the case with adaptive centroids, ELASTIC started at iterations n=500 (for $N_c = 4$) and n=1500 (for $N_c = 8$) and the joint adaptation was executed for a total of 2000 and 5000 iterations for comparing with the convergence levels achieved in figures 7.19(b) and 7.17(b). The results show an improvement in the I/O residual error of approximately 3dB and 2dB which is in accordance with the average improvements found in the long term tests and expressed in the curves of figure 7.14 for 4 and 8 centroids and similar values of IBO. In the case of 4 coefficients, we also observe that, as a result of centroid adaptation, the out-of-band behaviour is different featuring higher PD components (in dotted line) and a lower out-of-band PSD level for the corrected signal at Rx (also depicted using dotted line).

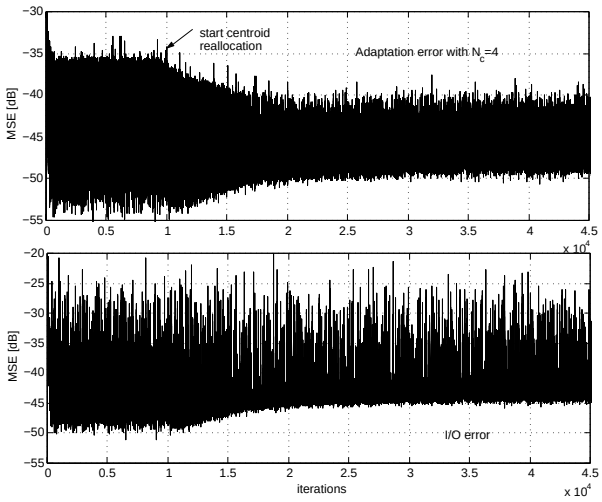

(a) Effect of the centroid reallocation on the MSE

Figure 7.25: In this figure we exemplify a case where the use of centroid reallocation leads to almost the same mean residual error level but improves the density of peak errors. A reduced number of $N_c = 4$ coefficients were used and the centroid adaptation started at iteration $n = 10000$. Although this improvement is not easily observable when we analyze the average behaviour of the residual error spectrum, it is important to consider that the peak errors will be associated to data transmission errors according to the selected modulation level. Therefore, long-term BER measurements would be necessary to evaluate quantitatively the benefits of reducing the peak error density.

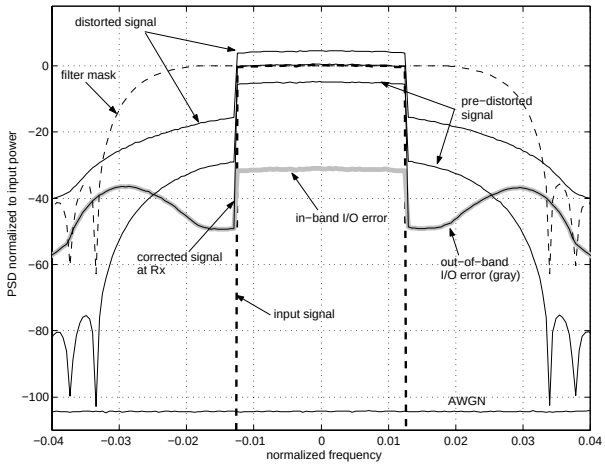

Figure 7.26: In this test we included a square root raised cosine filter for $\mathbf{h}_1$, with a roll-off factor of 0.3. Here we observe two important effects. First, the influence of the band limitation imposed by the filter to the correction bandwidth: the out-of-band I/O error is low where the filter response is flat allowing the PD components to pass to the HPA input (note that the I/O error arises as the PD components are eliminated by the filter). Second, a significant difference is observed in the compensation of the in-band residual error which is higher within the correction bandwidth. This negative effect is due to the uncompensated fractional delays introduced by filtering (see figure 7.28 of input-to-output mapping) and should be corrected by including adaptive filters to assure fine synchronization.

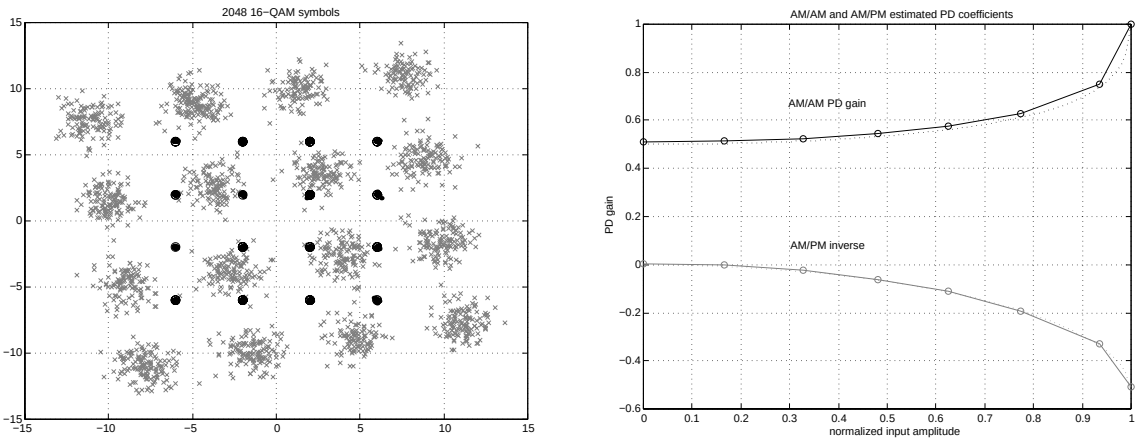

(a) (b)

Figure 7.27: (a) 16-QAM symbol constellation associated to the same PD test of figure 7.26. (b) Estimated AM/AM and AM/PM PD coefficients for the test in figure 7.26. Note that the AM/AM PD gain coefficients estimated are approximately uniformly biased with respect to the theoretical PD curve. This occurs due to the lack of time alignment in constructing the adaptation error signal. Under these conditions a linear attenuation factor is included when filtering and the algorithm tends to compensate for it through the PD coefficients.

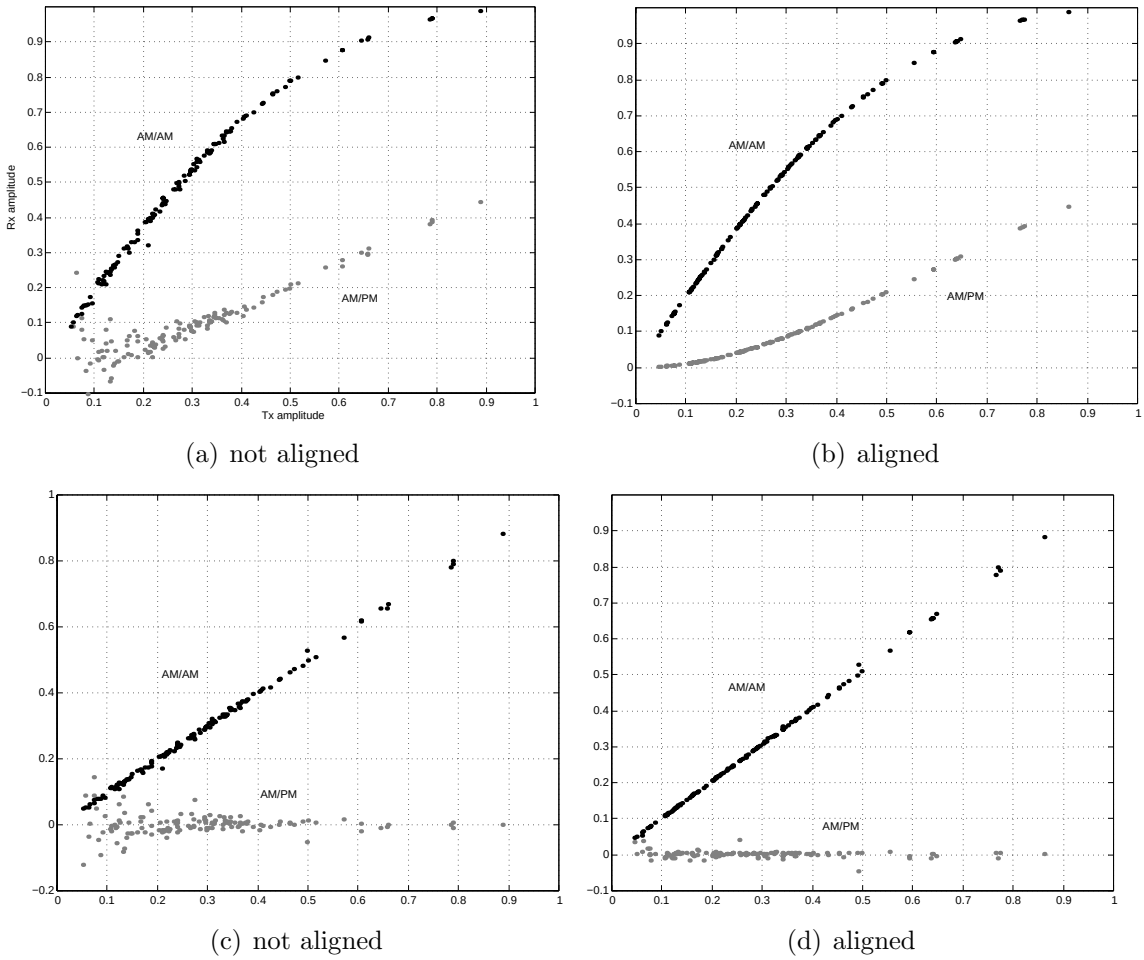

(a) not aligned

(b) aligned

(c) not aligned

(d) aligned

Figure 7.28: I/O mappings with filtering observed in the system of figure 7.5. In (a) and (b) we respectively observe the I/O mappings for $|\mathbf{b}_{dist}|$ vs. $|\mathbf{b}_{in}|$ (AM/AM) and for $\phi = \arg\{\mathbf{b}_{dist}\} - \arg\{\mathbf{b}_{in}\}$ vs. $|\mathbf{b}_{in}|$ (AM/PM) obtained at the lower branch where no PD has been applied. Similarly, in (c) and (d) we observe the I/O mappings resulting at the linearized chain (upper branch) between $\mathbf{b}_{in}$ and $\mathbf{b}_{out}$. The time-aligned maps are obtained considering the delay-compensation block embedding the linear components used to observe the the I/O error as shown in figure 7.4. The unaligned maps are obtained by observing the same output signals $\mathbf{b}_{dist}$ and $\mathbf{b}_{out}$ but now related to the input signal at the output of the IFFT. Note that the compensation block for fractional delays is used only to observe the I/O error and not to train the coefficients. Therefore the trained coefficients consider the time misalignment which is evidenced in the higher in-band error observed from the PSD results shown in figure 7.26.

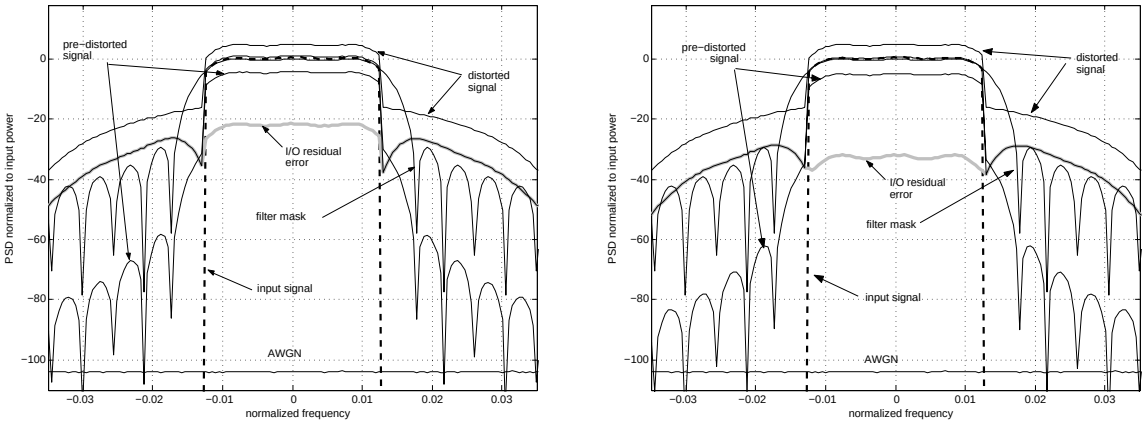

(a) not aligned (b) aligned

Figure 7.29: In these figures, the same signal and settings of figure 7.26 have been applied except for the filter characteristics which have been changed (to a narrower bandwidth with a roll-off factor of 0.7) in order to observe the degradation in PD results when the the out-of-band pre-correction components are filtered. We observe in (a) that the outermost active sub-carriers and the pre-correction bandwidth are affected by the rapid decrease of the filter response. As a result of this, the pre-distorted signal spectrum is bandlimited to the HPA input resulting in a relatively good compensation near the edges of the input signal band followed by an important increment of the out-of-band error which is governed by the filter response. Besides this, we observe that the residual error spectrum abruptly changes at the border between out-of-band and in-band frequency regions. This negative effect is due to the uncompensated fractional delays still present during the PD training and error signal monitoring. In the construction of the adaptation error signal $\mathbf{e} = \mathbf{b}_x - \mathbf{b}_p$ used in figure 7.4 we apply a coarse time alignment with an integer sample time resolution. However, the fractional delays introduced at the analog part of the chain are not compensated by this block. Therefore, we replaced the coarse alignment by an almost exact time alignment by including the same block of linear components used in the I/O error branch instead of the block ΔT_s at the adaptation error branch. The result is shown in (b) where we observe how the in-band error is reduced in approximately 10dB thus compensating for the severe difference between in-band and out-of-band errors obtained in (a). In light of this, we conclude that the next step to improve the PD scheme, for a more complete model of a real transmission chain, must include adaptive filters or interpolators for the fine synchronization of the signal streams used to estimate the PD coefficients.

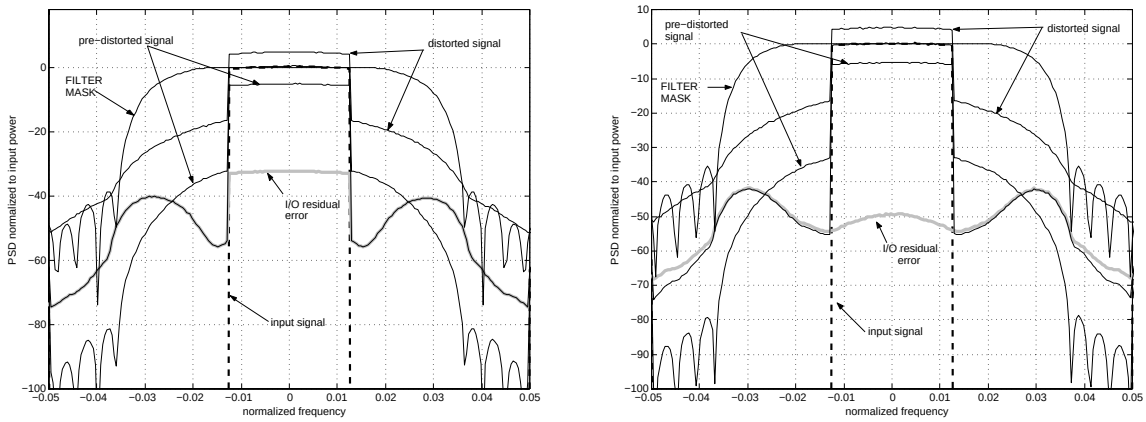

(a) not aligned (b) aligned

Figure 7.30: Effect of time alignment on the in-band I/O error using $N_c = 16$ coefficients. Both tests were carried out in the systems of figures 7.4 and 7.5 with $\mathbf{h}_1$ active. The frequency response of the filter is shown in the figure for a a roll-off factor of 0.4 to assure unitary gain at the active band and a slow attenuation of the pre-correction bandwidth. The input signal has an IBO= 9.8dB and the modulation scheme used was 16-QAM. The result in (a) shows the unacceptable in-band I/O error level resulting from the inadequate PD estimation achieved using only coarse time alignment (sample time resolution) to construct the adaptation error signal used to train the PD coefficients. In turn, the result in (b) feature a more acceptable I/O error level These results can be compared with the illustrative example shown previously in figure 7.29 for 4 coefficients. In this case we considered a higher number of coefficients and more suitable characteristics for the filter. Moreover, the reduction of the in-band residual error is now of approximately 16dB since an almost ideal time alignment was applied and, therefore, the PD coefficients were correctly trained. The data correction results and estimated PD coefficients obtained are shown next in figure 7.31.

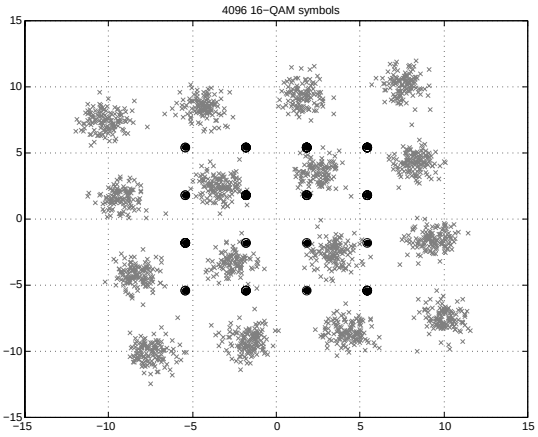

(a) not aligned

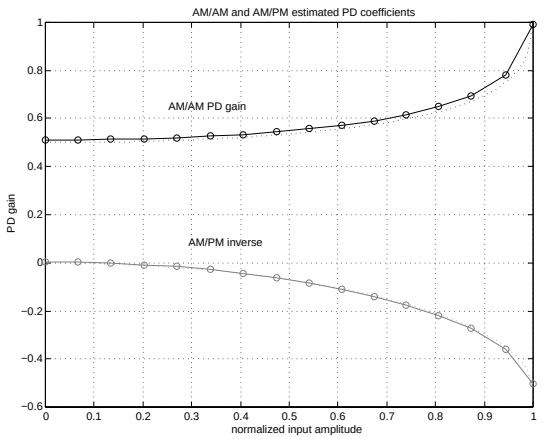

(b) not aligned

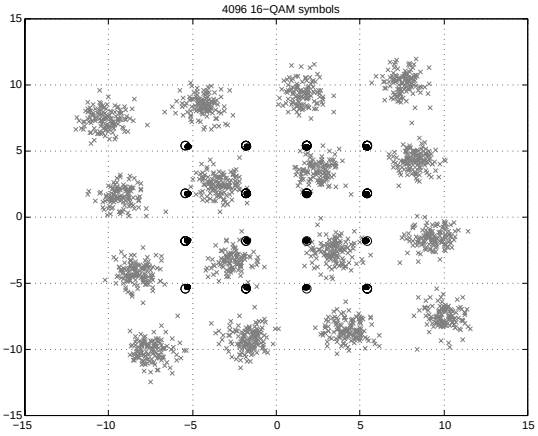

(c) aligned

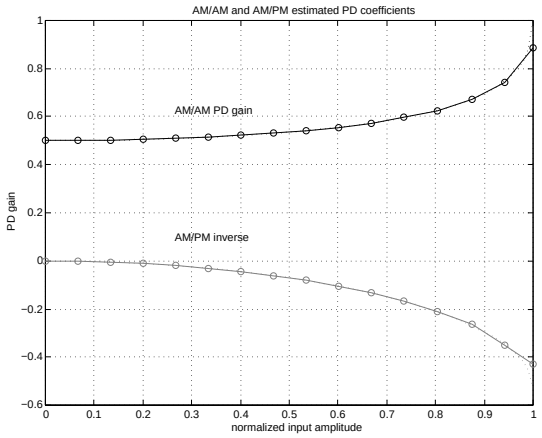

(d) aligned

Figure 7.31: Symbol constellation and estimated PD coefficients for the test of figure 7.30. Note that the in-band correction achieved with time alignment is much more noticeable from the spectral results than by observing the received data. Now, in figures (b) and (d), we note a uniform difference in the estimated AM/AM gain coefficients. Here, for the training with non-synchronous data streams, the estimated PD coefficients result uniformly biased along the input range.